

Gaia-DR2 distance to the W3 Complex in the Perseus Arm

Felipe Navarete^{1*}, Phillip A. B. Galli² and Augusto Damineli¹

¹*Universidade de São Paulo, Instituto de Astronomia, Geofísica e Ciências Atmosféricas, Rua do Matão, 1226, 05508-090, Brazil.*

²*Laboratoire d'astrophysique de Bordeaux, Univ. Bordeaux, CNRS, B18N, allée Geoffroy Saint-Hillaire, 33615 Pessac, France.*

Accepted XXX. Received YYY; in original form ZZZ

ABSTRACT

The Perseus Arm is the closest Galactic spiral arm from the Sun, offering an excellent opportunity to study in detail its stellar population. However, its distance has been controversial with discrepancies by a factor of two. Kinematic distances are in the range 3.9-4.2 kpc as compared to 1.9-2.3 kpc from spectrophotometric and trigonometric parallaxes, reinforcing previous claims that this arm exhibits peculiar velocities. We used the astrometric information of a sample of 31 OB stars from the star-forming W3 Complex to identify another 37 W3 members and to derive its distance from their *Gaia*-DR2 parallaxes with improved accuracy. The *Gaia*-DR2 distance to the W3 Complex, $2.14^{+0.08}_{-0.07}$ kpc, coincides with the previous stellar distances of ~ 2 kpc. The *Gaia*-DR2 parallaxes tentatively show differential distances for different parts of the W3 Complex: W3 Main, located to the NE direction, is at $2.30^{+0.19}_{-0.16}$ kpc, the W3 Cluster (IC 1795), in the central region of the complex, is at $2.17^{+0.12}_{-0.11}$ kpc, and W3(OH) is at $2.00^{+0.29}_{-0.23}$ kpc to the SW direction. The W3 Cluster is the oldest region, indicating that it triggered the formation of the other two star-forming regions located at the edges of an expanding shell around the cluster.

Key words: HII regions – infrared: stars – stars: early type – stars: distances – stars: fundamental parameters

1 INTRODUCTION

The Milky Way is a benchmark to understand the structure and evolution of spiral galaxies in details. However, the position of the Solar system, embedded into the Galactic disc, makes it difficult to determine the precise structure of the spiral arms.

In the past decades, most of the Galactic spiral structure studies relied on the position and Galactocentric distance of different sources derived from their radial velocity and inferring a model for the Galactic rotation curve (e.g. the standard Galactic rotation curve based on hydrogen emission from H II regions by [Georgelin & Georgelin 1976](#) and [Brand & Blitz 1993](#); star-forming complexes by [Russeil 2003](#), high-mass star-forming regions from [Reid et al. 2014](#); and red clump giants from [López-Corredoira 2014](#)). Recently, [Reid et al. \(2014, 2016\)](#) reported a view of the spiral structure of the Milky Way based on distances derived from trigonometric parallaxes of masers in high-mass star-forming regions. A complementary view of the Galactic spiral structure, based on the molecular content of high-mass star-forming regions, is presented by [Urquhart et al. \(2014\)](#), see their Fig. 6). [Hou & Han \(2014\)](#) combined the data ob-

tained for a large number of H II regions, giant molecular clouds and 6.7 GHz methanol masers to derive a comprehensive model for the galactic rotation curve and spiral arms distribution. Up-to-date, the above-mentioned works correspond to the most accurate Galactic rotation curve models available in the literature.

The assumption of a Galactic rotation model (commonly referred as kinematic method) relies upon several assumptions of the geometry and motion of the Galactic disc. For instance, the orbits are assumed to be circular, and deviations from circular orbits are often induced by dynamical processes in the Galaxy, such as the propagation of winds from high-mass stars ([Kudritzki & Puls 2000](#)), shocks from supernovae explosions ([Zhou et al. 2016](#)), or fluctuations in the gravitational potential ([Junqueira et al. 2013](#)). The combination of these effects can result in large non-circular velocities, leading to unrealistic farther kinematic distance determinations. The catalogue of Galactic complexes of H II regions from [Moisés et al. \(2011\)](#) indicates that half of the structures have kinematic distances larger by a factor of two than their corresponding non-kinematic distances, mostly derived from spectrophotometric analysis and trigonometric parallaxes.

Spectrophotometric distances are often obtained through spectral type classification of stars using photome-

* E-mail: navarete@usp.br (FN)

try and spectroscopy in the optical or near-infrared (NIR) (e.g. [Hanson et al. 1996](#), [Moisés et al. 2011](#)). This method requires a reasonable modelling of the interstellar medium reddening and an accurate calibration for the spectral type of the stars (e.g. [Hanson et al. 2005](#)). The reddening and the spectral classification correspond to the major sources of uncertainty of the spectrophotometric technique. The scattering on the calibration of the absolute magnitudes of O-type stars ($\Delta K = \pm 0.67$ mag) translates into an error of 30% over the distance of each source ([Blum et al. 2000](#)). The uncertainty on the reddening arises from the impossibility of evaluating the local interstellar medium (ISM) for each region. Since there are different reddening laws available in the literature (e.g. [Cardelli et al. 1989](#), [Stead & Hoare 2009](#) and [Damineli et al. 2016](#)), two extremes are often adopted for obtaining a mean reddening correction and its uncertainty.

On the other hand, distances derived from annual trigonometric parallaxes are not dependent on any modelling of stellar or ISM parameters, offering a direct estimate of the distance to the source. In the past decades, Very Long Baseline Interferometry (VLBI) observations have been used to measure the parallax of maser sources with unprecedented accuracy (of about 3%, [Xu et al. 2006](#)). The available angular resolution of VLBI measurements (about 0.01 milliarcseconds at 22 GHz, [Hachisuka et al. 2006](#)) have favoured the study of the Galactic spiral structure based on bright maser sources.

The Perseus arm is the nearest spiral arm from the Sun, located at the Galactic anti-centre direction. The complex of H II regions W3 (hereafter, W3 Complex) is one of the most prominent star-forming regions located in the second Galactic quadrant ($\ell \sim 130^\circ$) and associated with the Perseus arm, offering an excellent opportunity to determine the distance to this spiral arm using both kinematic and non-kinematic methods.

The W3 Complex is located in between the famous Heart and Soul nebulae, in the Cassiopeia constellation. The nebulae are powered by the W5 and W4+W3 radio sources, respectively, and covers a region of about 5.5×4 degrees in the sky. These active star-forming H II regions trace the Perseus spiral arm in the Galactic anti-centre direction. The existence of at least three stellar clusters – IC 1848 in W5 ([Hoag et al. 1961](#)), IC 1805 in W4 ([Vasilevskis et al. 1965](#)), and IC 1795 in W3 ([Ogura & Ishida 1976](#)) – combined to the relatively low ISM extinction makes this site strategic to study the formation of massive stars because its distance is prone to be determined with high accuracy.

Previous non-kinematic distances to these stellar clusters, especially IC 1805 (in W4), indicate values in the range of 2.3–2.4 kpc ([Kwon & Lee 1983](#); [Massey et al. 1995](#); [Sung et al. 2017](#)), while the distance to IC 1848 (W5) ranges from 1.9 to 2.2 kpc ([Becker & Fenkart 1971](#); [Georgelin & Georgelin 1976](#); [Chauhan et al. 2011](#)). Also, the kinematic distance to W5, $d \sim 3$ kpc, is about 1.5 times larger than its stellar distances ([Ginsburg et al. 2011](#)).

The distance to the W3 complex was derived from its stellar content in the optical ([Humphreys 1978](#)) and in the near-infrared ([Navarete et al. 2011](#)), leading to values around $d \sim 2.2$ kpc, in agreement with the non-kinematic distances to W4 and W5. The distance to W3 was also derived by using high-angular resolution from VLBI observations to measure the trigonometric parallaxes of maser emis-

Table 1. Distances to W3 reported in the literature.

Method	Range	Region	d (kpc)	Ref.
Spectrophotometric	Optical	b	2.18	H78
Spectrophotometric	Optical	no info.	2.30 ± 0.25	R03
Spectrophotometric	Infrared	a,b,c	$2.20^{+0.80}_{-0.64}$	N11
Trigonometric parallax	22 GHz	a	1.9 ± 0.3	I00
Trigonometric Parallax	22 GHz	c	2.04 ± 0.07	H06
Trigonometric parallax	Radio	c	1.95 ± 0.04	X06
Kinematic distance	Radio	c	$2.93^{+0.68}_{-0.63}$	R14
Kinematic distance	Radio	c	$3.81^{+0.96}_{-0.69}$	W18
Kinematic distance	Radio	no info.	$4.2^{+0.7}_{-0.6}$	R03

Notes: Regions: *a)* W3 Main; *b)* W3 Cluster; *c)* W3(OH). References: H78 – [Humphreys \(1978\)](#); I00 – [Imai et al. 2000](#); R03 – [Russeil 2003](#); H06 – [Hachisuka et al. 2006](#); X06 – [Xu et al. 2006](#); N11 – [Navarete et al. 2011](#); R14 – [Reid et al. 2014](#); W18 – [Wenger et al. 2018](#).

sion sources (e.g. H₂O or CH₃OH), leading to distances of $d \sim 2.0$ kpc ([Hachisuka et al. 2006](#); [Xu et al. 2006](#)). However, the kinematic distances to W3, ranging from 2.9 to 4.2 kpc ([Reid et al. 2014](#) and [Russeil 2003](#), respectively), are systematically larger than those obtained from the non-kinematic methods mentioned above. Table 1 summarises the distances reported in the literature for the W3 Complex. When available, the table also indicates the corresponding sub-structure of the W3 Complex studied in each case.

Most studies of the W3 Complex have focused on its high-density layer (HDL) (e.g. [Feigelson & Townsley 2008](#); [Navarete et al. 2011](#); [Bik et al. 2012](#)), which is believed to be the result of the expansion of the H II region driven by the cluster IC 1805 (i.e. the Heart Nebula), located in W4, into the W3 Giant Molecular Cloud (GMC) ([Lada et al. 1978](#)). The HDL of W3 comprises a variety of H II regions at different evolutionary stages, and a total of 105 OB-type stars were spectroscopically confirmed as W3 members ([Kiminki et al. 2015](#)). The W3 Complex corresponds to the central part of the HDL, and is divided into three main sub-structures: the central IC 1795 cluster, W3 Main located to the NW direction, and W3(OH) to the SE direction.

An O6.5 V star (BD+61 411) lies at the centre of the W3 Complex, corresponding to the main source of the IC 1795 cluster (hereafter, W3 Cluster). The W3 Cluster is the most prominent structure of the W3 Complex at optical wavelengths with a population of about 2,000 stellar objects ([Roccatagliata et al. 2011](#)), and is one of the oldest clusters ([Oey et al. 2005](#), 3–5 Myr,) within W3. The cluster is located at the central position of an expanding super-bubble with a radius of $\sim 9'$, suggesting that the feedback from its star-forming activity triggered the subsequent star-forming events on the other sub-structures, such as W3 Main and W3(OH) (see Fig. 2).

W3 Main is located to the NW direction of the W3 Cluster and is an extended star-forming region, exhibiting a large number of infrared sources and H II regions at different evolutionary stages. [Bik et al. \(2012\)](#) investigated the OB stellar population of W3 Main, identifying 15 OB stars with spectral types between O5 V and B4 V. Those authors derived an age spread of 2–3 Myr for the W3 Main region, where the most massive star (IRS 2) is already evolved while other high-mass YSOs (e.g. IRS N1) are still deeply embedded in ultra-compact H II regions. Moreover, [Bik et al. \(2012\)](#) reported that only in the hyper-compact H II region

IRS5 the early-type stars are still surrounded by circumstellar material. X-ray observations of the pre-main sequence population of W3 Main (Feigelson & Townsley 2008) indicate that the whole structure has a spherical distribution with an angular diameter of $\sim 12'$, about twice the size inferred from near-infrared maps.

W3(OH) is a slowly expanding shell-like H II region with velocities of $3\text{--}5\text{ km s}^{-1}$ (Kawamura & Masson 1998), located to the SE direction of the W3 Complex. This region is well-known regarding its stellar population (Bik et al. 2012) and maser emission (Menten et al. 1988; Ojha et al. 2004; Hachisuka et al. 2006; Xu et al. 2006). The presence of early B-type stars at the Main Sequence (Navarete et al. 2011 and Kiminki et al. 2015) indicates that W3(OH) had a relatively recent star formation episode.

Thanks to the second release of the *Gaia* mission (hereafter, *Gaia*-DR2, Gaia collaboration et al. 2016, 2018), accuracy values closer to those obtained with VLBI measurements in the radio domain is now extended for targets visible at optical wavelengths. Indeed, the parallax errors for individual sources in the W3 Complex ranges from 0.02 to 0.16 milli-arcseconds (mas). In this study, we used the *Gaia*-DR2 measurements of the W3 Complex OB stellar population to infer a more precise distance to that region and to disentangle the distances to the sub-regions within the W3 Complex.

This manuscript is organised as follows. In Sect. 2, we present the sample of known OB stars in the literature associated with the W3 Complex and new candidate members selected in our analysis. In Sect. 3, we analyse the *Gaia*-DR2 parallaxes and we determine the distance to the W3 Complex, together with the evaluation of the distance to each sub-region of the complex. In Sect. 4, we compare our results with previous studies. Our conclusions are summarised in Sect. 5.

2 DATA

2.1 Known members of the OB stellar population of W3

A total of 48 OB stars within the W3 Complex, centred at RA = 02:26:32.4, Decl. = +62:00:27 and covering a $\sim 20' \times 20'$ region, were investigated and classified by Navarete et al. (2011), Bik et al. (2012) and Kiminki et al. (2015) and their properties are listed in Table 2.

The majority of sources (the numbers are given in parenthesis) are found within the three main sub-structures of the W3 Complex: W3 Main (10), W3 Cluster (8), and W3(OH) (4). The last 9 OB stars were classified as field stars associated with the HDL region. Although these objects are confirmed members of the W3 complex, they are not likely associated with any of the former sub-structures.

The cross-match between the sources listed in Table 2 with the *Gaia*-DR2 catalogue can lead to doubtful associations since the positions of both lists are not given for the same epoch. Fortunately, the *Gaia*-DR2 provides the cross-match between its sources with external large dense surveys, including the *Two Micron All-Sky Survey* (2MASS, Skrutskie et al. 2006). Thus, we used the 2MASS IDs listed in Table 2 to search for the corresponding *Gaia*-DR2 coun-

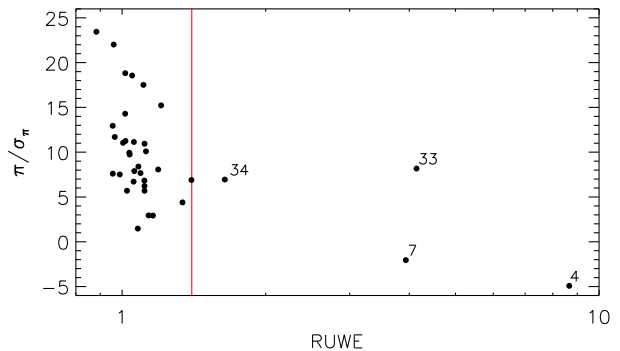


Figure 1. Parallax over the error (π/σ_π) versus the Re-normalised Unit Weight Error (RUWE) of the *Gaia*-DR2 sources. The vertical red line is placed at RUWE = 1.4, and the labelled sources were excluded from the analysis due to their large RUWE values.

terparts in the TMASS_BEST_NEIGHBOUR table of the *Gaia*-DR2 archive. Then, we downloaded the *Gaia*-DR2 data from the main catalogue. From the initial list of 48 OB stars, only 36 sources have complete information in the *Gaia*-DR2 catalogue (i.e. position, proper motion and parallax) required for the present study. The resulting list is presented in Table 3 and the *Gaia*-DR2 sources are indicated in Fig. 2, together with the vectors indicating the direction and magnitude of their proper motions.

We followed the recommendation of Lindegren et al. (2018b), we checked the goodness of the astrometric solution of each source by evaluating the re-normalised unit weight error parameter (RUWE), and keeping only those sources with $\text{RUWE} \leq 1.4$. Figure 1 presents the parallax over error ratio (π/σ_π) as a function of the RUWE parameter for all the *Gaia*-DR2 objects in the sample. The distribution of the points indicates that the adopted criterion was sufficient to separate sources with good astrometric solutions from those associated with either negative parallaxes or relatively large uncertainties (#4, #7, #33 and #34, see Fig. 1). In addition, the source #22 was also excluded from the sample due to the large uncertainty on its parallax ($\pi = 0.97 \pm 0.66$ mas). These procedures led to a final sample of 31 OB stars with reliable *Gaia*-DR2 parallaxes measurements.

Figure 2 exhibits the large-scale K_s -band map (at $2.16\ \mu\text{m}$) of the central $20' \times 20'$ region of the W3 Complex, extracted from the 2MASS image archive¹. The *Gaia*-DR2 sources are overlaid on the map, together with the vectors indicating the direction and magnitude of their proper motions.

Figure 3 presents the cumulative distribution of the proper motions in the right ascension and declination axis, and the parallaxes of the OB stars. The distributions of the proper motions are shifted towards negative values, indicating that most of the *Gaia*-DR2 sources are moving in the NW direction. The parallaxes are located within 0.3 and 0.7 mas, and the naive inversion of their individual values leads to distances in the range of 1.4–3.3 kpc.

We evaluated the weighted mean mean astrometric pa-

¹ <https://irsa.ipac.caltech.edu/applications/2MASS/IM/>

Table 2. Known OB stars associated with the W3 Complex.

ID	Source	RA (J2000)	DEC (J2000)	Spectral Type	Region	Ref.	2MASS	Offset (")
1	J02251857+6201169	02:25:18.6	+62:01:17.2	O5-O7 V	W3 Main	K15	02251857+6201169	0.07
2	IRS N8	02:25:26.3	+62:06:07.4	YSO	Field	K15	02252633+6206075	0.01
3	[NFD2011] 390	02:25:27.4	+62:03:43.2	B0-2 V	W3 Main	N11	02252738+6203432	0.11
4	[NFD2011] 559	02:25:28.1	+62:05:39.6	O7 V	W3 Main	N11	02252810+6205395	0.22
5	IRS 4	02:25:31.0	+62:06:20.6	O8-B0.5 V	W3 Main	B12	–	–
6	J02253167+6203249	02:25:31.7	+62:03:25.2	B1 V	W3 Main	K15	02253167+6203249	0.00
7	IRS N2	02:25:32.6	+62:06:59.8	B1-B2 V	W3 Main	B12	02253258+6206596	0.12
8	IRS N5	02:25:32.7	+62:05:08.1	B1-3 V	W3 Main	K15	02253274+6205079	0.59
9	J02253461+6201401	02:25:34.6	+62:01:40.3	B7 V	W3 Main	K15	02253461+6201401	0.19
10	IRS N1	02:25:35.1	+62:05:34.5	B2-3 V	W3 Main	B12	02253517+6205348	0.04
11	[NFD2011] 386	02:25:37.5	+62:05:24.8	B0-B2 V	W3 Main	N11	02253750+6205244	0.09
12	IRS 3a	02:25:37.8	+62:05:51.8	O5-7 V	W3 Main	B12	02253778+6205522	0.04
13	J02253880+6208168	02:25:38.8	+62:08:17.0	B2 V	W3 Main	K15	02253880+6208168	0.11
14	IRS 7	02:25:40.5	+62:05:39.8	O9-B2 V	W3 Main	B12	–	–
15	IRS N7	02:25:40.6	+62:05:46.8	YSO	W3 Main	K15	02254062+6205470	0.00
16	IRS 5	02:25:40.8	+62:05:52.3	YSO	W3 Main	K15	–	–
17	IRS 2b	02:25:41.7	+62:06:24.2	B0-1 V	W3 Main	B12	–	–
18	IRS 2a	02:25:43.3	+62:06:15.7	O8-O9 V	W3 Main	B12	02254334+6206154	0.08
19	IRS 2	02:25:44.3	+62:06:11.4	O6.5-7.5 V	W3 Main	B12	–	–
20	[NFD2011] 347	02:25:44.9	+62:03:41.5	B0-2 V	W3 Main	N11	02254485+6203413	0.17
21	J02254488+6208155	02:25:44.9	+62:08:15.8	B4-5 V	W3 Main	K15	02254488+6208155	0.12
22	IRS 2c	02:25:47.1	+62:06:13.0	B0-1 V	W3 Main	B12	02254709+6206131	0.06
23	J02254720+6153430	02:25:47.2	+61:53:43.3	B3-5 V	Field	K15	02254720+6153430	0.09
24	IRS N6	02:25:47.4	+62:06:55.3	B4 V	W3 Main	K15	02254748+6206543	0.03
25	J02255220+6156120	02:25:52.2	+61:56:12.3	B:	Field	B12	02255220+6156120	0.13
26	J02260587+6158465	02:26:05.9	+61:58:46.7	B1.5 V	W3 Cluster	K15	02260587+6158465	0.17
27	J02260729+6202550	02:26:07.3	+62:02:55.1	A1 V	Field	B12	02260729+6202550	0.19
28	J02261050+6158018	02:26:10.5	+61:58:02.0	B3 V	W3 Cluster	K15	02261050+6158018	0.15
29	J02261690+6207350	02:26:16.9	+62:07:35.2	B:	Field	K15	02261690+6207350	0.13
30	J02261880+6159529	02:26:18.8	+61:59:53.1	B4 V	W3 Cluster	K15	02261880+6159529	0.16
31	J02262290+6200370	02:26:22.9	+62:00:37.3	B1-2 V	W3 Cluster	K15	02262290+6200370	0.09
32	J02262442+6200501	02:26:24.4	+62:00:50.4	B4-6 V	W3 Cluster	K15	02262442+6200501	0.09
33	J02263433+6201527	02:26:34.3	+62:01:53.0	B4-5 V	W3 Cluster	K15	02263433+6201527	0.13
34	[NFD2011] 159	02:26:34.4	+62:00:42.4	O6.5 V	W3 Cluster	N11	02263440+6200426	0.25
35	[OWK2005] 1007	02:26:41.3	+61:59:24.6	B2 V	W3 Cluster	K15	02264129+6159242	0.02
36	J02264173+6158503	02:26:41.7	+61:58:50.6	B4-5 V	W3 Cluster	K15	02264173+6158503	0.10
37	J02264570+6159504	02:26:45.7	+61:59:50.7	B6-7 V	W3 Cluster	K15	02264570+6159504	0.07
38	[OWK2005] 4012	02:26:46.7	+62:00:26.2	B2 V	W3 Cluster	K15	02264664+6200259	0.06
39	J02265627+6206313	02:26:56.3	+62:06:31.5	B0-3 V	Field	K15	02265627+6206313	0.10
40	J02270938+6154437	02:27:09.4	+61:54:44.0	B1-3 V	W3(OH)	K15	02270938+6154437	0.08
41	J02271290+6151390	02:27:12.9	+61:51:39.2	B1-2 V	W3(OH)	B12	02271290+6151390	0.07
42	J02271510+6200151	02:27:15.1	+62:00:15.3	B2 V	Field	B12	02271510+6200151	0.11
43	J02271602+6200506	02:27:16.0	+62:00:50.8	B:	Field	K15	02271602+6200506	0.15
44	J02272023+6202023	02:27:20.3	+62:02:02.6	B0-1.5 V	Field	K15	02272023+6202023	0.05
45	[NFD2011] 252	02:27:21.4	+61:54:57.3	B1-B4 V	W3(OH)	N11	02272133+6154570	0.04
46	[NFD2011] 3	02:27:34.6	+61:55:57.2	B0-IIIe	W3(OH)	N11	02273459+6155571	0.06
47	J02273953+6156330	02:27:39.6	+61:56:33.3	B0-B2 V	W3(OH)	K15	02273953+6156330	0.06
48	J02274017+6204197	02:27:40.2	+62:04:20.0	B1-4 V	Field	K15	02274017+6204197	0.07

Notes: the columns are as follows: (1) ID of the source; (2) identification of the OB star based on the name given in the referenced catalogues; (3) right ascension; (4) declination; (5) spectral type; (6) association with a sub-region of the W3 Complex; (7) references for the properties of the OB stars: N11 – Navarete et al. 2011; B12 – Bik et al. 2012; K15 – Kiminki et al. 2015; (8) 2MASS counterpart; (9) offset between the *Gaia*-DR2 and the 2MASS counterpart.

rameters of W3 and its sub-regions as:

$$\langle p \rangle = \sum_{i=1}^n w_i p_i \quad (1)$$

where the weight, w_i , is defined in terms of the uncertainty of the parameter p :

$$w_i = \frac{\sigma_{p,i}^{-2}}{\sum_{i=1}^n \sigma_{p,i}^{-2}} \quad (2)$$

The error of the weighted mean was obtained by considering the uncertainty on each measurement of the parameter and the spatial correlation between the position of the stars:

$$\sigma_{\langle p \rangle}^2 = \sum_{i=1}^n \sum_{j=1}^n (w_i \sigma_{p,i}) \cdot (w_j \sigma_{p,j}) \cdot V(\theta_{ij}) \quad (3)$$

where $V(\theta_{ij})$ is the spatial covariance function between

Table 3. Gaia-DR2 information of the OB-type stellar population of the W3 Complex.

ID	Designation (<i>Gaia</i> DR2 #)	sep ($''$)	α (deg)	δ (deg)	$\mu_{\alpha} \cos(\delta)$ (mas yr $^{-1}$)	μ_{δ} (mas yr $^{-1}$)	μ (mas yr $^{-1}$)	π (mas)	G (mag)	[BP-RP] (mag)	RUWE
1	513638063807365248	0.07	36.327350	62.021349	-1.388 ± 0.071	-1.817 ± 0.091	2.29 ± 0.12	0.423 ± 0.062	14.21	3.60	1.11
3	513638579203426816	0.11	36.364035	62.061969	-2.380 ± 0.056	-2.611 ± 0.071	3.53 ± 0.09	0.379 ± 0.048	15.02	2.96	1.08
4	513638922800802048	0.22	36.367054	62.094276	1.294 ± 0.453	-0.520 ± 0.546	1.39 ± 0.71	-1.890 ± 0.384	13.19	2.91	8.56 *
6	513638510483951232	0.07	36.381921	62.056924	-0.983 ± 0.029	-1.035 ± 0.037	1.43 ± 0.05	0.452 ± 0.024	13.82	2.23	1.03
7	513638957160533888	0.12	36.385753	62.116530	0.728 ± 0.389	-2.747 ± 0.480	2.84 ± 0.62	-0.704 ± 0.343	16.29	3.83	3.90 *
9	513637376612594688	0.19	36.394190	62.027765	-0.797 ± 0.044	-0.916 ± 0.055	1.21 ± 0.07	0.366 ± 0.038	15.78	1.92	1.03
11	513638751002110336	0.09	36.406259	62.090096	-0.508 ± 0.171	-1.647 ± 0.197	1.72 ± 0.26	0.420 ± 0.143	17.40	4.15	1.15
13	513662459222193536	0.11	36.411647	62.137995	-1.168 ± 0.052	-0.961 ± 0.067	1.51 ± 0.08	0.374 ± 0.046	15.34	2.37	1.21
18	513662218697964928	0.08	36.430548	62.104269	0.250 ± 0.172	-3.855 ± 0.200	3.86 ± 0.26	0.687 ± 0.156	17.49	3.39	1.34
20	513637892008658048	0.17	36.436857	62.061437	-0.196 ± 0.061	-2.212 ± 0.077	2.22 ± 0.10	0.413 ± 0.054	14.17	3.23	1.08
21	513662562301408384	0.12	36.436991	62.137638	-0.639 ± 0.043	-0.061 ± 0.056	0.64 ± 0.07	0.413 ± 0.037	15.74	2.00	1.01
22	513662149984550912	0.06	36.446185	62.103628	-0.331 ± 0.794	-2.509 ± 0.977	2.53 ± 1.26	0.973 ± 0.662	20.19	3.41	1.08 *
23	513632119572654848	0.09	36.446698	61.895264	-0.575 ± 0.055	-0.454 ± 0.073	0.73 ± 0.09	0.346 ± 0.052	15.98	2.31	1.05
24	513662180045929728	0.25	36.447991	62.115128	-0.773 ± 0.185	-0.648 ± 0.220	1.01 ± 0.29	0.472 ± 0.161	17.88	3.63	1.16
25	513633871919302016	0.13	36.467507	61.936648	-1.369 ± 0.039	-0.323 ± 0.052	1.41 ± 0.06	0.399 ± 0.034	15.60	1.93	0.96
26	513634387315470848	0.17	36.524411	61.979552	-1.030 ± 0.034	-0.010 ± 0.048	1.03 ± 0.06	0.439 ± 0.029	14.14	2.10	1.21
27	513661050473012992	0.19	36.530359	62.048567	-0.557 ± 0.033	0.126 ± 0.046	0.57 ± 0.06	0.432 ± 0.030	15.17	1.56	1.02
28	513634181157041792	0.15	36.543749	61.967146	-0.312 ± 0.044	-0.626 ± 0.063	0.70 ± 0.08	0.511 ± 0.039	15.82	2.18	0.96
29	513661905166430080	0.13	36.570399	62.126359	-0.648 ± 0.085	-0.613 ± 0.114	0.89 ± 0.14	0.491 ± 0.079	15.76	3.37	1.12
30	513634352955730816	0.16	36.578321	61.998003	-0.652 ± 0.027	0.101 ± 0.040	0.66 ± 0.05	0.468 ± 0.025	14.67	1.61	1.01
31	513657820657620864	0.08	36.595387	62.010258	-0.694 ± 0.035	-0.487 ± 0.054	0.85 ± 0.06	0.372 ± 0.033	14.38	2.37	1.03
32	513657820657620736	0.09	36.601735	62.013918	-0.807 ± 0.073	-0.357 ± 0.112	0.88 ± 0.13	0.381 ± 0.067	15.99	2.88	1.12
33	513657889377083520	0.13	36.642966	62.031299	-2.307 ± 0.098	1.795 ± 0.127	2.92 ± 0.16	0.738 ± 0.090	14.03	1.35	4.39 *
34	513657786292622848	0.28	36.643312	62.011764	-0.455 ± 0.071	0.575 ± 0.087	0.73 ± 0.11	0.393 ± 0.057	9.89	1.43	1.87 *
35	513656961664153728	0.02	36.672069	61.990061	-0.645 ± 0.022	-0.090 ± 0.034	0.65 ± 0.04	0.452 ± 0.021	13.88	1.40	1.01
37	513657064743367552	0.07	36.690397	61.997331	-0.669 ± 0.059	-0.636 ± 0.084	0.92 ± 0.10	0.304 ± 0.053	15.89	2.21	1.02
38	513657064743365760	0.06	36.694330	62.007184	-0.522 ± 0.021	0.094 ± 0.031	0.53 ± 0.04	0.441 ± 0.019	13.51	1.44	0.93
39	513660019680852992	0.10	36.734476	62.108671	-0.655 ± 0.048	-0.692 ± 0.067	0.95 ± 0.08	0.479 ± 0.043	14.90	2.68	1.07
40	513609373425115136	0.07	36.789058	61.912138	-0.979 ± 0.061	-0.070 ± 0.089	0.98 ± 0.11	0.456 ± 0.060	16.22	2.67	0.96
41	513585046729657216	0.07	36.803742	61.860829	-1.339 ± 0.030	-0.031 ± 0.044	1.34 ± 0.05	0.485 ± 0.028	13.66	2.19	1.11
43	513610404217453312	0.15	36.816736	62.014023	-0.317 ± 0.070	-0.571 ± 0.098	0.65 ± 0.12	0.615 ± 0.061	14.40	3.29	1.13
44	513610438576963712	0.05	36.834264	62.033991	-0.113 ± 0.051	0.245 ± 0.070	0.27 ± 0.09	0.510 ± 0.047	14.81	2.67	1.13
45	513608754949821952	0.04	36.838890	61.915831	-0.867 ± 0.069	-0.506 ± 0.099	1.00 ± 0.12	0.465 ± 0.062	15.66	3.39	0.99
46	513609098547198720	0.06	36.894142	61.932525	-0.986 ± 0.091	0.165 ± 0.131	1.00 ± 0.16	0.569 ± 0.083	14.27	3.54	1.37
47	513609132906935168	0.06	36.914674	61.942501	-0.726 ± 0.074	-0.589 ± 0.103	0.93 ± 0.13	0.546 ± 0.065	15.78	3.15	1.06
48	513612397082030720	0.07	36.917376	62.072145	-0.273 ± 0.058	-0.501 ± 0.080	0.57 ± 0.10	0.500 ± 0.050	16.10	2.33	1.03

Notes: The columns are as follows: (1) ID from Table 2; (2) Designation from the *Gaia*-DR2 DR2 catalogue; (3) angular separation between the 2MASS and the *Gaia*-DR2 coordinates; (4) right ascension of the *Gaia*-DR2 source (in decimal degrees); (5) declination of the *Gaia*-DR2 Source (in decimal degrees); (6) proper motion on the α -axis and its error; (7) proper motion on the δ -axis and its error; (8) total proper motion and its error; (9) parallax and its error from the *Gaia*-DR2-DR2 archive; (10) *G*-band magnitude; (11) *BP-RP* colour index; (12) Re-normalised Unit Weight Error (RUWE); (13) sources flagged with an * were removed from the analysis based on the RUWE selection criterion ($\text{RUWE} \leq 1.4$) to remove sources with poor astrometry.

sources i and j , defined as:

$$V(\theta_{ij}) = A \cdot \exp\left(-\frac{\theta_{ij}}{\Delta\ell}\right) \quad (4)$$

with θ_{ij} being the angular separation between sources i and j , $A=1$ (for $i=j$, $V(\theta)=1$), and $\Delta\ell=0.5^\circ$ is defined by Lindegren et al. (2018a). The weighted mean proper motion of the OB stellar population is -0.786 ± 0.055 and -0.520 ± 0.062 mas yr $^{-1}$ and the mean parallax is $\langle\pi\rangle=0.442 \pm 0.041$ mas (with no zero-point correction, see Sect. 4.1). These values are indicated in Fig. 3 as the solid and dashed lines.

2.2 New members of the W3 Complex based on *Gaia*-DR2 data

We selected a larger sample of candidate members of the W3 Complex based on the astrometric parameters of the well-known OB stars present in the same region. At first,

we have selected all the 2249 *Gaia*-DR2 sources located within the FOV presented in Fig. 2 which also satisfied the $\text{RUWE} \leq 1.4$ criterion (see Sect. 2.1). Then, we narrowed the sample to 99 sources by selecting only those objects with proper motions within the range between $\pm 5\sigma$ from the weighted mean proper motion values of the OB stars, that is, $-1.06 \leq \mu_{\alpha} \cos(\delta) \leq -0.51$ mas yr $^{-1}$ and $-0.83 \leq \mu_{\delta} \leq -0.21$ mas yr $^{-1}$.

These sources were associated with parallaxes with a larger distribution range (from -1.6 to 1.3 mas) when compared to the parallaxes of the OB stars (0.30 to 0.69 mas). Thus, selected only those objects with parallax measurements within a 3σ limit from the weighted mean parallax value (i.e. $0.319 \leq \pi \leq 0.565$ mas), leading to a sample of 45 objects. This selection contains eight of the sources listed in Table 3 and 37 new objects. Table 4 lists the properties of the 37 additional *Gaia*-DR2 objects. The association between the 31 confirmed members of the W3 complex and

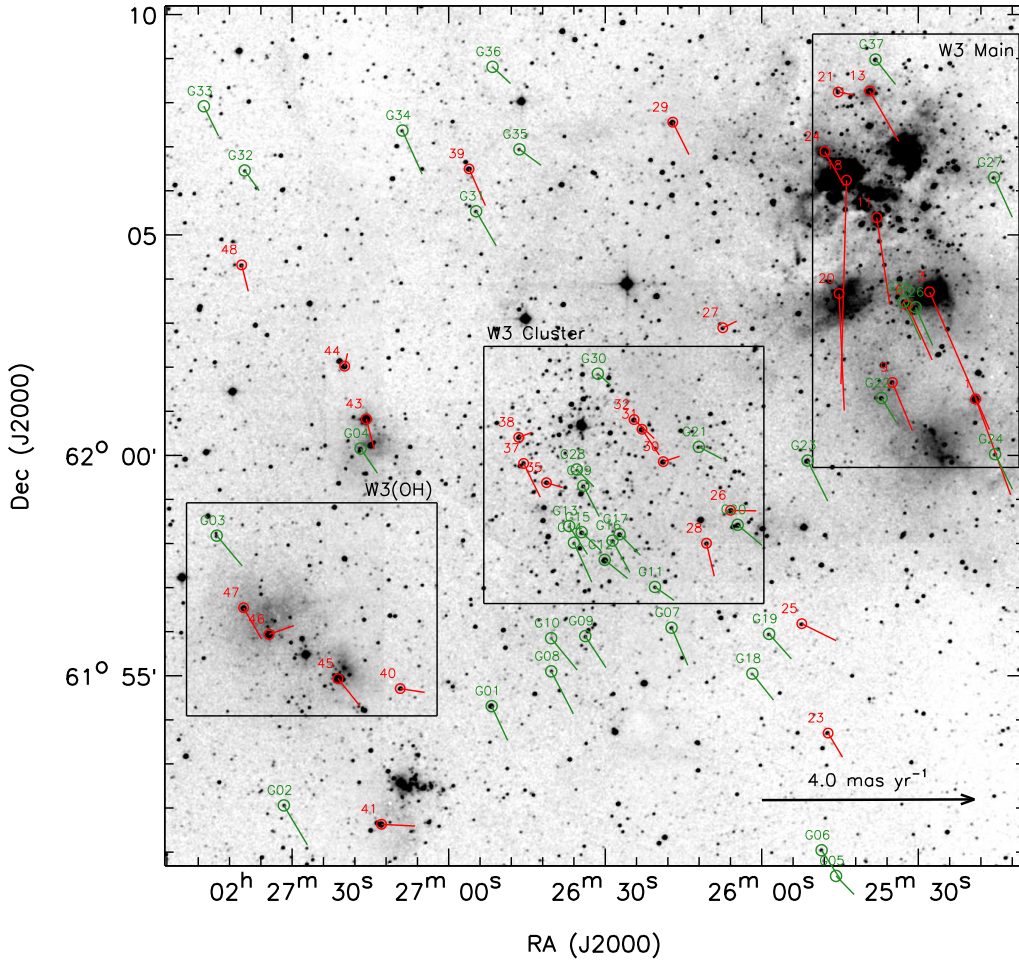


Figure 2. *K*-band map of the W3 complex (centred at RA = 02:26:32.4, Decl. = +62:00:27) overlaid by the OB stellar population with astrometry available in the *Gaia*-DR2 catalogue. The red circles indicate the position of the OB stars (labelled using the IDs from Table 2), and the arrows indicate the direction and magnitude of their proper motions (a scale is indicated by the black arrow at the bottom right corner of the map). The green circles indicate the position of *Gaia*-DR2 objects with similar astrometric parameters as the OB stars and candidate members of the W3 Complex (see Sect. 2.2). The black rectangles indicate the location of the W3 Main, W3 Cluster and W3(OH). North is up, and East is to the left.

the 37 new candidates selected based on the criteria defined above lead to a final sample of 68 *Gaia*-DR2 sources.

We performed a two-sample Kolmogorov-Smirnov test to check test whether the two distributions are different (i.e. the OB star population – see Sect 2 – and the *Gaia*-DR2 selected sources – see Sect. 2.2). The samples are considered statistically different if their KS rank factor is close to 1 and associated with a probability value, p smaller than 0.05 (p -values of 0.05, 0.002 and <0.001 represent the ~ 2 -, 3- and >3 - σ confidence levels). The results are summarised in Table 5. We found that the KS rank factors are about ~ 0.3 for the proper motions, indicating a relatively small difference between the distribution of the OB stars and the sources listed in Table 4. The KS rank factor for the parallax is even smaller, $KS=0.12$ and associated with a high p -value ($p=0.95$), indicating a non-significant difference between each distribution. These results support that both the known OB stellar population of W3 and the new *Gaia*-DR2

candidate members of W3 are similar in terms of their astrometric information.

Finally, we associated the new sample of 68 stars with the sub-regions of the W3 Complex by using the same position criteria indicated in Fig. 2. We found that 16 sources are within W3 Main, 20 are associated with W3 Cluster, five are located in W3(OH), and 27 are likely not associated with any of the former sub-structures (field stars).

3 RESULTS

3.1 Systematic effects on *Gaia*-DR2-parallaxes

According to Lindegren et al. (2018b), the systematic errors in the *Gaia*-DR2 parallaxes are estimated to be less than 0.1 mas. The published uncertainties of the *Gaia*-DR2 parallaxes correspond to internal errors only and do not consider systematic or external errors (Lindegren et al. 2018b,a). By following the recommendation of Lindegren et al. (2018a),

Table 4. *Gaia*-DR2 data of the new W3 members selected in this study.

ID	Designation (<i>Gaia</i> DR2 #)	W3 region	α (deg)	δ (deg)	$\mu_\alpha \cos(\delta)$ (mas yr ⁻¹)	μ_δ (mas yr ⁻¹)	μ (mas yr ⁻¹)	π (mas)	G (mag)	[BP-RP] (mag)	RUWE
G01	513586146241283072	d	36.715834	61.905581	-0.637 ± 0.034	-0.644 ± 0.048	0.91 ± 0.06	0.406 ± 0.031	12.81	1.46	0.95
G02	513608273913499008	d	36.881812	61.867867	-0.950 ± 0.123	-0.747 ± 0.158	1.21 ± 0.20	0.458 ± 0.109	17.40	2.63	1.05
G03	513609266046952192	b	36.936479	61.969724	-1.029 ± 0.133	-0.572 ± 0.158	1.18 ± 0.21	0.537 ± 0.110	17.59	2.57	1.06
G04	513610301138022528	d	36.821306	62.002882	-0.683 ± 0.035	-0.469 ± 0.052	0.83 ± 0.06	0.505 ± 0.032	15.24	1.65	1.17
G05	513630775244268288	d	36.440729	61.841246	-0.722 ± 0.206	-0.352 ± 0.293	0.80 ± 0.36	0.362 ± 0.191	18.41	3.67	1.04
G06	513631157500074752	d	36.452212	61.850967	-0.737 ± 0.083	-0.542 ± 0.120	0.92 ± 0.15	0.481 ± 0.078	16.95	2.48	0.99
G07	513632978566202624	d	36.571849	61.935235	-0.647 ± 0.147	-0.711 ± 0.181	1.96 ± 0.23	0.514 ± 0.125	17.69	2.81	1.05
G08	513633047285680000	d	36.668163	61.918736	-0.885 ± 0.327	-0.803 ± 0.409	1.20 ± 0.52	0.443 ± 0.261	19.04	2.96	0.99
G09	513633111711389824	d	36.640956	61.932075	-0.829 ± 0.192	-0.598 ± 0.247	1.02 ± 0.31	0.369 ± 0.176	18.45	2.82	0.99
G10	513633146067364736	d	36.668250	61.931271	-1.041 ± 0.642	-0.600 ± 0.763	1.20 ± 1.00	0.551 ± 0.579	20.01	2.36	1.07
G11	513633356523322624	c	36.585116	61.950644	-0.767 ± 0.187	-0.255 ± 0.255	0.81 ± 0.32	0.496 ± 0.168	18.27	2.74	1.08
G12	513633425242797568	b	36.625383	61.960912	-0.917 ± 0.206	-0.354 ± 0.281	0.98 ± 0.35	0.415 ± 0.179	18.08	4.00	1.07
G13	513633455302772864	b	36.653876	61.973686	-0.735 ± 0.383	-0.540 ± 0.441	0.91 ± 0.58	0.408 ± 0.311	19.27	2.50	1.02
G14	513633459597914112	b	36.649997	61.967404	-0.715 ± 0.313	-0.748 ± 0.400	1.03 ± 0.51	0.508 ± 0.274	19.00	2.89	1.02
G15	5136334520456485632	b	36.643851	61.971339	-0.774 ± 0.078	-0.350 ± 0.108	0.85 ± 0.13	0.407 ± 0.070	16.90	2.58	0.93
G16	513633489662505472	b	36.619071	61.968168	-0.696 ± 0.227	-0.603 ± 0.303	0.92 ± 0.38	0.474 ± 0.201	18.55	2.61	1.10
G17	513633493962273152	b	36.613435	61.970601	-0.840 ± 0.058	-0.402 ± 0.083	0.93 ± 0.10	0.357 ± 0.052	16.05	2.60	1.02
G18	513633597036933504	b	36.507163	61.917826	-0.841 ± 0.441	-0.501 ± 0.567	0.98 ± 0.72	0.491 ± 0.352	19.51	2.92	0.99
G19	513633665760970752	b	36.493734	61.932811	-0.889 ± 0.126	-0.473 ± 0.154	1.01 ± 0.20	0.354 ± 0.106	17.56	2.50	1.00
G20	513634387315471232	b	36.518742	61.974081	-0.982 ± 0.056	-0.392 ± 0.078	1.06 ± 0.10	0.468 ± 0.049	15.63	2.79	0.99
G21	513634520456485632	b	36.549796	62.003578	-0.917 ± 0.210	-0.226 ± 0.285	0.94 ± 0.35	0.366 ± 0.183	18.47	2.54	1.03
G22	513637307893119232	a	36.402893	62.021857	-0.591 ± 0.039	-0.462 ± 0.049	0.75 ± 0.06	0.464 ± 0.034	15.61	1.81	0.97
G23	513637410972338432	d	36.462507	61.998311	-0.807 ± 0.056	-0.767 ± 0.070	1.11 ± 0.09	0.453 ± 0.049	15.71	2.59	1.07
G24	513637960728155264	d	36.312037	62.000456	-0.692 ± 0.109	-0.664 ± 0.129	0.96 ± 0.17	0.356 ± 0.096	17.40	2.57	1.00
G25	513638510483950976	a	36.385138	62.058260	-0.700 ± 0.054	-0.722 ± 0.066	1.01 ± 0.09	0.479 ± 0.046	16.22	2.07	0.99
G26	513638510483952256	a	36.375288	62.056131	-0.677 ± 0.112	-0.722 ± 0.131	0.99 ± 0.17	0.458 ± 0.093	17.42	2.68	1.00
G27	513650639471583616	a	36.311688	62.105059	-0.723 ± 0.173	-0.753 ± 0.213	1.04 ± 0.27	0.343 ± 0.150	18.20	3.02	1.02
G28	513656996023891584	b	36.647729	61.995069	-0.689 ± 0.472	-0.326 ± 0.595	0.76 ± 0.76	0.551 ± 0.377	19.41	2.63	1.07
G29	513656996023892864	b	36.642495	61.988897	-0.638 ± 0.132	-0.582 ± 0.169	0.86 ± 0.21	0.342 ± 0.116	17.49	2.63	1.01
G30	513657958096560512	b	36.630819	62.031292	-0.530 ± 0.600	-0.223 ± 0.540	0.57 ± 0.81	0.429 ± 0.349	19.11	2.03	1.07
G31	513658473492629248	d	36.728785	62.092657	-0.812 ± 0.090	-0.656 ± 0.121	1.04 ± 0.15	0.541 ± 0.081	16.92	2.22	1.03
G32	513659435565297920	d	36.915298	62.107850	-0.586 ± 0.043	-0.381 ± 0.057	0.70 ± 0.07	0.511 ± 0.038	15.68	1.52	1.05
G33	513659572998812672	d	36.948379	62.132059	-0.594 ± 0.624	-0.561 ± 0.664	0.82 ± 0.91	0.409 ± 0.473	19.86	2.31	0.98
G34	513660122754670976	d	36.788270	62.123131	-0.800 ± 0.160	-0.824 ± 0.234	1.15 ± 0.28	0.516 ± 0.149	18.04	2.45	1.03
G35	513660225833910144	d	36.693976	62.116079	-0.869 ± 0.123	-0.299 ± 0.148	0.92 ± 0.19	0.531 ± 0.104	17.56	2.31	0.98
G36	513660363278230272	d	36.715726	62.147274	-0.729 ± 0.110	-0.318 ± 0.132	0.80 ± 0.17	0.540 ± 0.092	17.42	1.59	1.03
G37	513662631020884608	a	36.406787	62.149860	-0.799 ± 0.129	-0.473 ± 0.150	0.93 ± 0.20	0.397 ± 0.113	17.40	3.16	1.00

Notes: The columns are as follows: (1) ID of the Source; (2) Designation from the *Gaia*-DR2-DR2 catalogue; (3) Association with a sub-region of the W3 Complex: (a) W3 Main, (b) W3 Cluster, (c) W3(OH), or (d) field star. (3) right ascension of the *Gaia*-DR2 source (in decimal degrees); (4) declination of the *Gaia*-DR2 Source (in decimal degrees); (5) proper motion on the α -axis and its error; (6) proper motion on the δ -axis and its error; (7) total proper motion and its error; (8) parallax and its error from the *Gaia*-DR2-DR2 archive; (9) *G*-band magnitude; (10) *BP-RP* colour index; (11) Re-normalised Unit Weight Error (RUWE).

Table 5. Kolmogorov-Smirnov statistics between the astrometric parameters of the OB stellar population and the *Gaia*-DR2 candidate members of W3.

Parameter	π	$\mu_\alpha \cos(\delta)$	μ_δ	μ
KS	0.12	0.33	0.32	0.32
<i>p</i>	0.95	0.04	0.05	0.05

Notes: The KS test and its probability (*p*) are shown for each parameter. KS values closer to 1 and *p*-values smaller than 0.05 indicate that the distributions are significantly different.

the total uncertainty on the parallax, σ_π , is a combination of the internal parallax error (σ_i) and an external error (σ_e), given by:

$$\sigma_\pi = \sqrt{k^2 \sigma_i^2 + \sigma_e^2} \quad (5)$$

where $k = 1.08$, and σ_e depends on the brightness of the source ($\sigma_e = 0.021$ mas for $G \leq 13$ mag, and $\sigma_e = 0.043$ mas for $G > 13$ mag). Similarly, the total error of the proper mo-

tions and position were also evaluated using Eq. (5), with $\sigma_e = 0.033$ mas yr⁻¹ or 0.066 mas yr⁻¹ (and in case of the position, 0.016 mas or 0.033 mas) for $G \leq 13$ mag or $G > 13$ mag, respectively.

Another systematic effect in the *Gaia*-DR2 parallaxes corresponds to the existence of a global zero-point (ZP) correction of their values, which should be applied to all parallaxes before any further interpretation of their results. For the analysis of the W3 parallaxes, we adopted the ZP correction derived by Graczyk et al. (2019), $\pi_{ZP} = -0.031 \pm 0.011$ mas, based on the analysis of an all-sky sample of 81 galactic eclipsing binary stars. The effects of different ZP offsets on the *Gaia*-DR2 parallaxes are further discussed in Sect. 4.1).

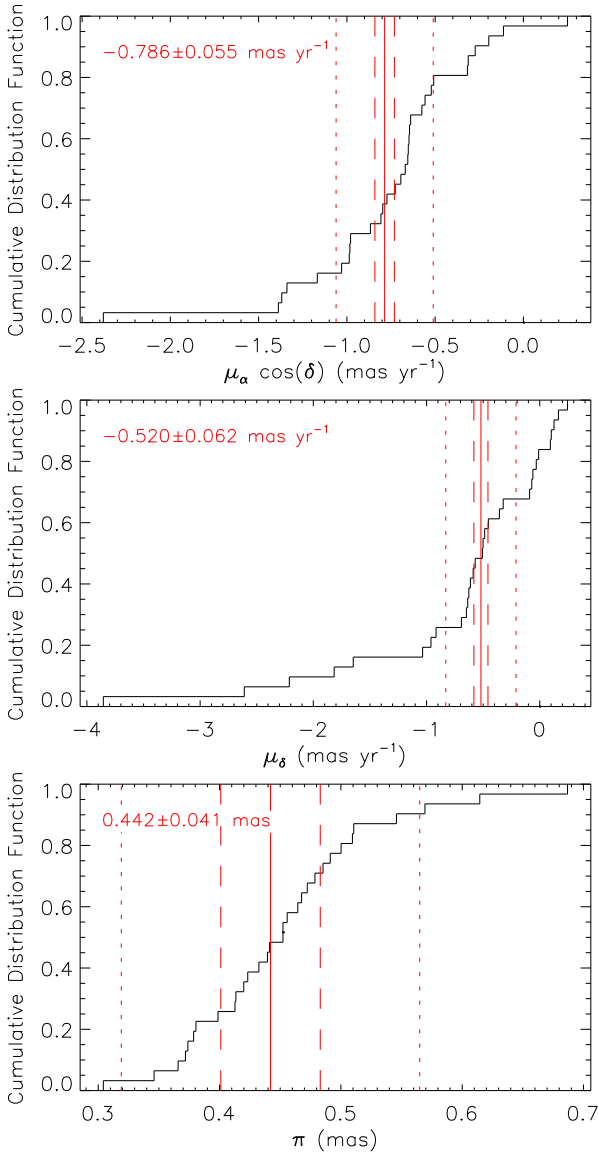


Figure 3. Cumulative distribution function of the astrometric parameters of the OB stars. The distribution of the proper motions in the right ascension and declination axis are presented in the top and middle panels, respectively, and the parallaxes in the bottom. The mean and its error from Table 6 are presented in the top left corner of each panel and are indicated by the solid and dashed vertical red lines, respectively. The threshold used for selecting the larger sample of *Gaia*-DR2 objects are indicated by the dotted red lines (corresponding to 5- and 3- σ for the proper motion and parallaxes, respectively).

3.2 Weighted mean astrometric parameters

After correcting for the global zero-point, the parallaxes of the stars ranged from 0.335 to 0.718 mas. Using Eqs. (1) and (3), we evaluated the weighted mean parallax of the W3 complex and its error as $\langle \pi \rangle = 0.473 \pm 0.041$ mas considering only the OB stars, and $\langle \pi \rangle = 0.477 \pm 0.044$ mas when considering the larger sample of 68 stars. Similarly, we obtained the weighted mean position and proper motions of the W3 and its sub-regions. These values are reported in Table 6, together with the corresponding distances using the

naive inversion of the parallaxes. However, the evaluation of distances by inverting parallaxes is only valid in the absence of uncertainties. That is not the case for *Gaia*-DR2 parallaxes since they have intrinsic uncertainties provided in the *Gaia*-DR2 catalogue and are also affected by systematic errors as previously mentioned in Sect. 3.1. For this reason, we adopted a Bayesian inference method to derive the distance to the W3 complex and its sub-structures. The description of this method and the results are presented as follows.

3.3 Distance to the W3 Complex

The distance to the W3 Complex and its sub-structures were calculated by following the tutorials provided in the *Gaia*-DR2 archive² (see, e.g. Luri et al. 2018, hereafter L18). We adopted the Exponentially Decreasing Space Density (EDSD) prior from Bailer-Jones (2015, hereafter, BJ15), given by:

$$P(r) = \frac{r^2}{2L^3} \exp\left(-\frac{r}{L}\right) \quad (6)$$

where r is the distance and L is the length scale of the distribution. We adopted the standard value $L = 1.35$ kpc from Astraatmadja & Bailer-Jones (2016), which was also used for estimating distances from *Gaia*-DR2-DR1 parallaxes. We note that the EDSD prior is appropriate for the general, old Galactic population, which has a different spatial Galactic distribution when compared to the young stellar population of the Galactic disc. For this reason, we tested our results using a self-gravitating, isothermal Galactic disc prior by Maíz-Apellániz (2001), based on the analysis of Hipparcos data of the Galactic OB stellar population. The tests indicate that the usage of one prior or another has not substantially changed our results (for details, see Appendix A). To account for the correlation between each member of the W3 complex, we used the *multiple-source Bayesian Inference* procedure from the *Gaia*-DR2 archive, which assumes that the position (α , δ), the parallax (π) and its error (σ_π) are correlated quantities.

Figure 4 exhibits the probability density function (PDF) of the distance to the W3 complex using the EDSD prior and considering all the 31 OB stars selected as described in Sect. 2.1. We note that the PDF exhibits a slight asymmetric profile, elongated towards larger distance values. For this reason, BJ15 and L18 adopted the median and a 90% confidence interval (5% and 95%) for evaluating the distance and its errors. However, the errors on the previous distance estimates for W3 are based on a 1- σ interval (roughly corresponding to a confidence interval of 68%). Therefore, we adopted a narrower, 68% confidence interval to better compare our results with those available in the literature (see Table 1).

The median value and the 1- σ (68%) confidence interval of the PDF shown in Fig. 4 correspond to the distance of $2.23^{+0.15}_{-0.14}$ kpc. This value is relatively larger than the distance derived from the naive inversion of the mean parallax of the OB stars, $d = 2.11^{+0.20}_{-0.17}$ kpc, shown as the solid red line in Fig. 4. We note that the accuracy of the distance evaluated using the *Gaia*-DR2 parallaxes and the Bayesian inference

² <https://gea.esac.esa.int/archive/>

Table 6. Mean parameters and distance to the W3 Complex and its main sub-regions based on the OB stars and the larger *Gaia*-DR2 sample.

OB stars								
Region	N	$\langle\alpha\rangle$ (deg)	$\langle\delta\rangle$ (deg)	$\langle\mu_\alpha \cos(\delta)\rangle$ (mas yr ⁻¹)	$\langle\mu_\delta\rangle$ (mas yr ⁻¹)	$\langle\pi\rangle$ (mas)	$\langle d\rangle$ (kpc)	d _{EDSD} (kpc)
W3	31	36.598 ± 0.029	62.011 ± 0.030	-0.786 ± 0.055	-0.520 ± 0.062	0.473 ± 0.041	2.11 ^{+0.20} _{-0.17}	2.23 ^{+0.15} _{-0.14}
W3 Main	10	36.398 ± 0.036	62.076 ± 0.036	-1.000 ± 0.066	-1.312 ± 0.073	0.444 ± 0.064	2.25 ^{+0.38} _{-0.28}	2.46 ^{+0.25} _{-0.21}
W3 Cluster	8	36.615 ± 0.030	61.995 ± 0.030	-0.661 ± 0.056	-0.179 ± 0.063	0.460 ± 0.055	2.17 ^{+0.29} _{-0.23}	2.07 ^{+0.18} _{-0.15}
W3(OH)	4	36.852 ± 0.045	61.924 ± 0.046	-0.889 ± 0.079	-0.28 ± 0.10	0.534 ± 0.078	1.87 ^{+0.32} _{-0.24}	2.00 ^{+0.30} _{-0.23}
Field	9	36.674 ± 0.030	61.996 ± 0.030	-0.706 ± 0.056	-0.249 ± 0.064	0.498 ± 0.055	2.01 ^{+0.25} _{-0.20}	2.19 ^{+0.23} _{-0.19}
Larger <i>Gaia</i> -DR2 sample								
Region	N	$\langle\alpha\rangle$ (deg)	$\langle\delta\rangle$ (deg)	$\langle\mu_\alpha \cos(\delta)\rangle$ (mas yr ⁻¹)	$\langle\mu_\delta\rangle$ (mas yr ⁻¹)	$\langle\pi\rangle$ (mas)	$\langle d\rangle$ (kpc)	d _{EDSD} (kpc)
W3	68	36.606 ± 0.032	62.005 ± 0.032	-0.767 ± 0.059	-0.528 ± 0.068	0.477 ± 0.044	2.10 ^{+0.21} _{-0.18}	2.14 ^{+0.08} _{-0.07}
W3 Main	16	36.382 ± 0.033	62.074 ± 0.033	-0.848 ± 0.061	-1.327 ± 0.068	0.458 ± 0.045	2.18 ^{+0.24} _{-0.20}	2.30 ^{+0.19} _{-0.16}
W3 Cluster	20	36.629 ± 0.029	61.996 ± 0.030	-0.696 ± 0.056	-0.132 ± 0.063	0.471 ± 0.040	2.12 ^{+0.20} _{-0.17}	2.17 ^{+0.12} _{-0.11}
W3(OH)	5	36.826 ± 0.035	61.921 ± 0.035	-0.779 ± 0.064	-0.226 ± 0.075	0.506 ± 0.048	1.98 ^{+0.21} _{-0.17}	2.00 ^{+0.29} _{-0.23}
W3 Field	27	36.717 ± 0.030	61.997 ± 0.030	-0.762 ± 0.055	-0.799 ± 0.064	0.504 ± 0.042	1.98 ^{+0.17} _{-0.15}	2.08 ^{+0.17} _{-0.10}

Notes: The columns are as follows: (1) sub-region of the W3 Complex; (2) number of sources; (3) mean right ascension and the corresponding error (in degrees); (4) mean declination and the corresponding error (in degrees); (5) mean proper motion on the right ascension direction and the corresponding error (in mas yr⁻¹); (6) mean proper motion on the declination direction and the corresponding error (in mas yr⁻¹); (7) mean parallax and the corresponding error (in mas); (8) distance inferred from the inversion of the mean parallax (in kpc); (9) distance (in kpc) inferred from the multiple-source Bayesian Inference method (see Sect. 3.3).

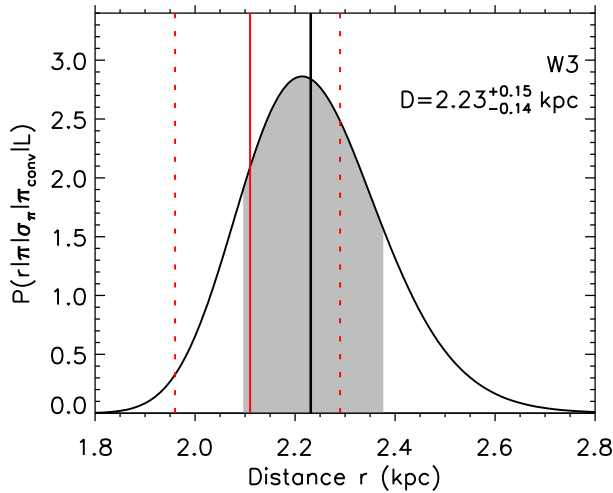


Figure 4. Probability density function (PDF) of the distance to the W3 Complex, based on the sample of OB stars. The median value of the PDF is indicated by the black vertical line. The errors correspond to the 1- σ (68%) confidence interval (shaded grey area). For comparison, the solid and dashed red lines indicate the distance and its error obtained from the naive inversion of the mean parallax reported in Table 6.

method is around 7% at 1- σ , closer to the accuracy of the distances derived from radio parallax measurements (about 3%, e.g. Hachisuka et al. 2006; Xu et al. 2006) than those obtained through, e.g., the spectrophotometric method (less accurate than 10%, see Table 1.)

Figure 5 presents the PDF of the distance to each sub-structure of the W3 complex, obtained using the EDSD prior and considering only the OB stars within the corresponding black box presented in Fig. 2. The distances derived from the PDFs are listed in Table 6. In the top panel, we present the PDF of the distance to W3 Main, located in the NW region of the W3 Complex (see Fig. 2). The PDF exhibits

a broad profile, extending from 2.0 to \sim 3.2 kpc. The median and the 1- σ confidence interval of the PDF leads to the distance of $d = 2.46^{+0.25}_{-0.21}$ kpc. The distance to W3 Main is relatively larger than the distance inferred for the whole W3 Complex (overlaid as the blue curve), suggesting that this sub-region is likely located at the outer edge of the W3 Complex. The PDF of the distance to the W3 Cluster is offset towards smaller distances and is relatively narrower when compared to the observed for the W3 Main. The median and the 1- σ confidence interval of the PDF leads to the distance of $d = 2.07^{+0.18}_{-0.15}$ kpc to the W3 Cluster. The distribution probability of the distance to W3(OH) exhibits the broadest profile shown in Fig. 5, ranging from \sim 1.4 to \sim 2.9 kpc. The distance to W3(OH), $d = 2.00^{+0.30}_{-0.23}$ kpc, places this sub-region at the nearest side of the W3 complex. Compared to the other sub-regions, the larger errors on the distance of W3(OH) may be caused by the relatively small sample of stars (only four) with measured parallaxes. Finally, the PDF of the distance to the OB stars classified as field stars is shown in the bottom panel of Fig. 5. These stars are confirmed members of the W3 complex but are not clearly associated with the former sub-regions. Despite that, and assuming that these stars are indeed members of W3, their position and parallaxes are still correlated. The distance derived from their PDF is $d = 2.19^{+0.23}_{-0.19}$ kpc.

Figure 6 presents the PDFs of the distances based on the larger sample of 68 *Gaia*-DR2 objects (see Sect. 2.2). The plots also indicate the distances and their errors obtained using the OB stars and presented in Figs. 4 and 5. The top panel indicates that the distance to the W3 Complex is $d = 2.14^{+0.08}_{-0.07}$ kpc when considering the larger sample. we found that the distance using the larger sample is determined with higher accuracy (from \sim 7 to \sim 4%) when compared to the distance obtained with the OB stars, $d = 2.23^{+0.15}_{-0.14}$ kpc (see Fig. 4).

As previously found in Fig. 5, the distances to each sub-region of the W3 Complex using the large sample of *Gaia*-

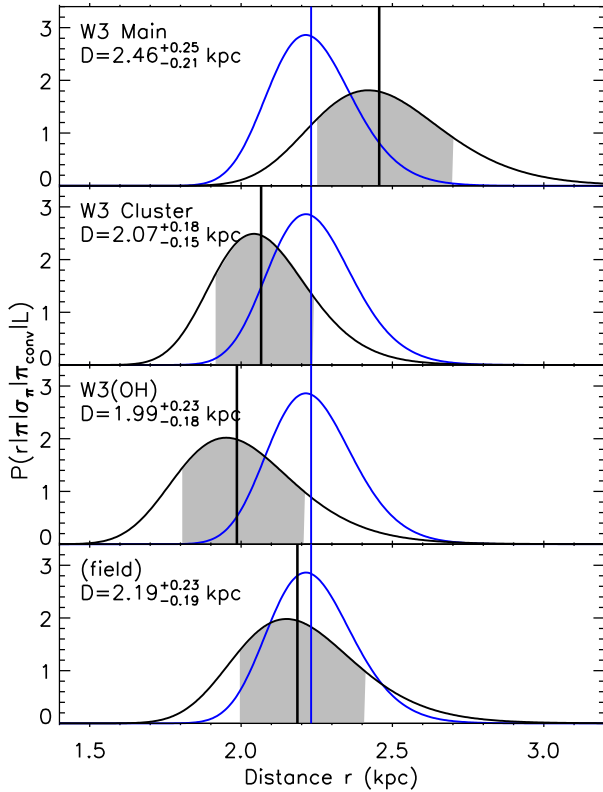


Figure 5. PDF of the distance to each sub-region of the W3 Complex, based on the sample of OB stars. From top to bottom: W3 Main, W3 Cluster, W3(OH), and sources located out of the regions above. The distance and its errors are derived from the median of the PDF (vertical line) and the $1\text{-}\sigma$ (68%) confidence interval (shaded area). For comparison, the PDF considering all the OB stars and its median distance are presented as the blue curve and the vertical blue line, respectively.

DR2 objects also indicate that they are located at different positions within the high-density layer of W3: W3(OH) is at the inner edge of the W3 Complex, at $2.00^{+0.29}_{-0.23}$ kpc; W3 Cluster is at the central region at $2.17^{+0.12}_{-0.11}$ kpc; and W3 Main is at the far, outer edge of the W3 Complex, at $d = 2.30^{+0.19}_{-0.16}$ kpc.

4 DISCUSSION

Previous works have reported the distance to the W3 Complex based on the individual distances of a few stellar objects (e.g. [Humphreys 1978](#); [Navarete et al. 2011](#)), or based on the trigonometric parallax of maser sources (e.g. [Xu et al. 2006](#); [Hachisuka et al. 2006](#)) located in W3(OH). The trigonometric parallax is the most direct estimate of the distance to an object and does not require any assumptions. On the other hand, methods such as the spectrophotometric analysis require a good interpretation of the physical parameters of the sources and the conditions of the interstellar medium in the line-of-sight. The *Gaia*-DR2 second data release offers the unique opportunity to derive the distance to the W3 Complex in the optical range with closer accuracy of the distances obtained through trigonometric parallax of masers in the GHz regime ($\sim 3\%$, e.g. [Hachisuka et al. 2006](#)

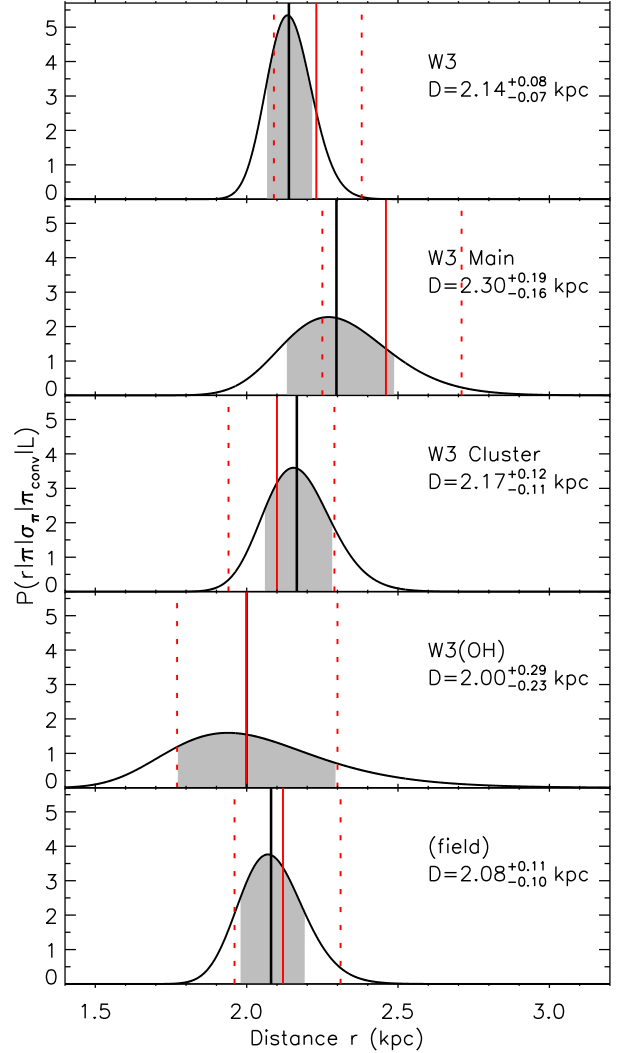


Figure 6. PDF of the distance to the W3 Complex and its sub-regions based on the larger sample of *Gaia*-DR2 sources located in the following regions (from top to bottom): the whole sample (W3), W3 Main, W3 Cluster, W3(OH), and sources located out of the regions above (field). The distance and its errors are derived from the median of the PDF (vertical line) and the $1\text{-}\sigma$ (68%) confidence interval (shaded area). In each panel, the median distance and its error derived using the OB stars are indicated by the solid and dashed lines, respectively.

and [Xu et al. 2006](#)). Despite of that, we note that the accuracy achieved by *Gaia*-DR2 is still not high enough for beating, for example, the quality of VLBI trigonometric parallax measurements. By the time *Gaia*-DR3 or DR4 arrives, the accuracy of their measurements might be similarly accurate or even surpass the VLBI measurements.

The distances derived from the Bayesian inference method using the Exponentially Decreasing Space Distribution prior from BJ15 are systematically larger than those obtained from the naive inversion of the weighted mean parallaxes (see [Table 6](#)). The adoption of other priors, such as the self-gravitating isothermal Galactic disc from [Maíz-Apellániz \(2001\)](#) leads to similar distances than those derived using the EDSB prior (see [Appendix A](#)). As our final results, we adopted the distances derived using the larger

Table 7. Global zero-point offsets available in the literature for *Gaia*-DR2 parallaxes.

ZP offset (mas)	Sources	Reference
-0.030	QSOs (all sky)	Lindegren et al. (2018b)
-0.031(11)	Eclipsing Binaries (all sky)	Graczyk et al. (2019)
-0.046(14)	Cepheids (all sky)	Riess et al. (2018)
-0.050(03)	RC stars (Kepler field ¹)	Zinn et al. (2018)
-0.053(03)	RGB stars (Kepler field ¹)	Zinn et al. (2018)
-0.056(11)	<i>Gaia</i> -DR2 RV sample	Schönrich et al. (2019)
-0.073(34)	YSOs in Orion ²	Kounkel et al. (2018)
-0.082(33)	Eclipsing Binaries (all sky)	Stassun & Torres (2018)

Notes: When available, the errors on the last two digits are given within the parenthesis. The central position of the fields are: 1) RA=19h23m, Decl=+44d30'; 2) RA=05h40m, Decl=-10d00'.

sample of *Gaia*-DR2 W3 members (Sect. 2.2), the EDSO prior and the Bayesian inference method, since it takes the uncertainties of the individual parallax measurements into account, and this prior has been widely used by the *Gaia* team. In Sect. 4.1, we further discuss the influence of the zero-point correction of the *Gaia*-DR2 parallaxes on our results. The analysis of the *Gaia*-DR2 parallaxes indicates that the sub-regions of the W3 Complex are likely located at different distances in our line-of-sight. These results are discussed in Sect. 4.2. Finally, we compare the distances to W3 based on the *Gaia*-DR2 parallaxes with previous estimates from the literature in Sect. 4.3.

4.1 Dependency of the zero-point correction on the distance determination

The major source of systematic errors on the *Gaia*-DR2 parallaxes is related to the zero-point correction. Lindegren et al. (2018b) reported that the *Gaia*-DR2 parallaxes are systematically smaller than the real values. They derived a zero-point correction of $\pi_{ZP} = -0.03$ mas, adopted by the *Gaia*-DR2 Team as the global ZP offset for the entire *Gaia*-DR2 catalogue. Despite that, recent works based on the study of different type of Galactic objects have reported larger ZP offsets, between -0.08 and -0.05 mas (e.g. Riess et al. 2018, Zinn et al. 2018 and Stassun & Torres 2018), suggesting that the parallaxes measured by the *Gaia*-DR2 are even smaller than predicted by Lindegren et al. (2018b).

More recently, Graczyk et al. (2019) analysed a sample of 81 eclipsing binaries with measured *Gaia*-DR2 parallaxes and obtained a global ZP offset of $\pi_{ZP} = -0.031 \pm 0.011$ mas, confirming the value suggested by Lindegren et al. (2018b). In Sect. 5 of Graczyk et al. (2019), those authors comment on the discrepancy of the ZP correction adopted by the *Gaia*-DR2 Team and those obtained by other authors. They claimed that such differences are either affected by systematic effects on the relations used for modelling the stellar parameters that are difficult to assess, or are merely specific for a particular region of the sky (e.g. Zinn et al. 2018 derived a ZP offset based on a sample of objects located in the *Kepler* field at RA \sim 19:23:00, Decl \sim +44:30:00). Table 7 summarises the recent *Gaia*-DR2 zero-point corrections available in the literature, together with the targets and the region of the sky used for each analysis.

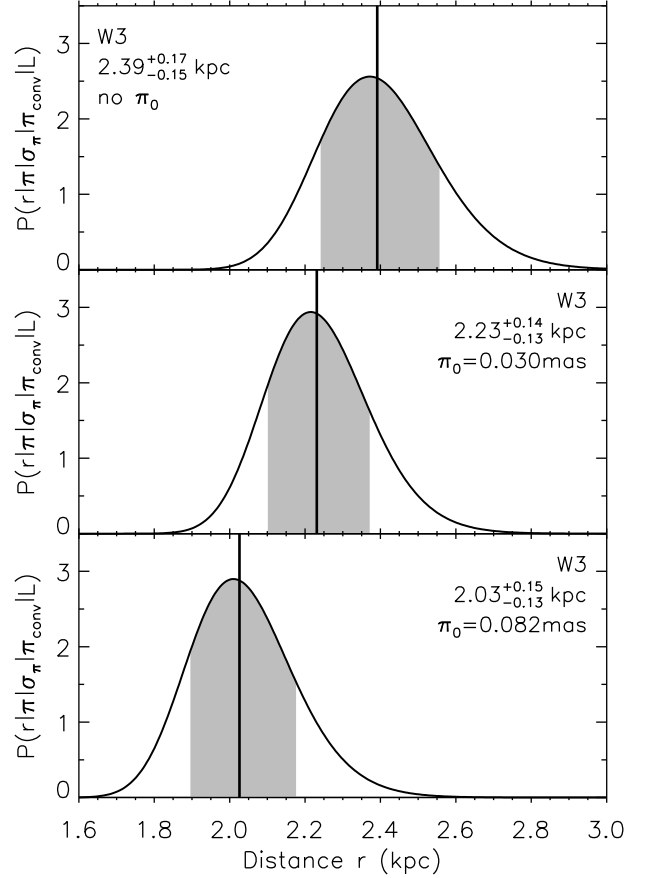


Figure 7. Probability density function (PDF) of the distance estimate with correlated parallaxes. The median value of the PDF is indicated by the black vertical line. The errors correspond to the $1\text{-}\sigma$ (68%) confidence interval (shaded grey area). Each PDF was obtained assuming different zero-point correction values: no ZP correction (top), zero-point correction of 0.03 mas (middle) and ZP correction of 0.082 ± 0.033 mas (bottom).

We further tested the influence of the ZP correction on the distance to the W3 Complex by using the parallaxes of all the OB stars listed in Table 6, and adopting three extreme cases: *a*) no ZP-correction, *b*) the ZP correction from Lindegren et al. (2018b, -0.030 mas), and *c*) the extreme case derived by Stassun & Torres (2018, $-0.082(33)$ mas).

Figure 7 presents the PDF of the distance to the W3 Complex after zero-point correcting using the offsets stated above. We found that the PDFs are systematically offset towards smaller distances as a function of the ZP value. The median distances and the $1\text{-}\sigma$ uncertainties are: *a*) $2.39^{+0.17}_{-0.15}$ kpc, *b*) $2.23^{+0.14}_{-0.13}$ kpc, and *c*) $2.03^{+0.15}_{-0.13}$ kpc. These results indicate that the ZP correction plays a critical role in the correct evaluation of the distances based on *Gaia*-DR2 parallaxes, especially for distances at kiloparsec scales, such as the case of W3.

4.2 The three dimensional structure of the W3 complex and its hierarchical star formation history

The analysis of the OB stellar population of the W3 Complex and its main sub-regions tentatively suggests that the high-

density layer of W3 exhibits a complex three-dimensional structure. The W3 Complex is elongated in the SE-NW direction, where the inner edge is represented by W3(OH) at $d = 1.99^{+0.23}_{-0.18}$ kpc, and the outer edge corresponds to the location of W3 Main, at $d = 2.46^{+0.25}_{-0.21}$ kpc. The W3 Cluster (IC 1795) is located at the central region of the complex, at $d = 2.07^{+0.18}_{-0.15}$ kpc. These results are confirmed with the analysis of a larger sample of 68 *Gaia*-DR2 sources, which includes the 31 OB stars and 37 new sources selected through astrometric information of the W3 Complex. When considering the larger sample, the distances to W3(OH), W3 Cluster and W3 Main are $d = 2.00^{+0.29}_{-0.23}$ kpc, $d = 2.17^{+0.12}_{-0.11}$ kpc, and $d = 2.30^{+0.19}_{-0.16}$ kpc, respectively.

The projected position on the sky combined with the distance of W3 Cluster places the oldest structure of the HDL (3-5 Myr Oey et al. 2005) at the centre of the W3 Complex. In a larger context, the three dimensional structure of the W3 Complex is consistent with the hierarchical scenario proposed by Oey et al. (2005) and Román-Zúñiga et al. (2015), who suggested that the W3 Cluster (IC 1795) triggered the star-forming process and consecutive formation of W3(OH) and W3 Main, located at the edges of a shell surrounding the W3 Cluster. These regions have ages of about 2-3 Myr (Navarete et al. 2011; Bik et al. 2012) and are actively forming stars (cf. Bik et al. 2012 and Román-Zúñiga et al. 2015). In addition, Oey et al. (2005) also suggested that the W3 Cluster formation was induced by an earlier burst of star formation in the W4 region, from which the first event of star formation occurred about 6-10 Myr ago.

4.3 The distance to W3 and the velocity discrepancy in the Perseus Arm

Figure 8 compares all the distance determinations for the W3 complex reported in Table 1 with those derived from the *Gaia*-DR2 parallaxes using the methodology of BJ15 (see last column of Table 6). The distances from the literature, reported in Table 1, are indicated right below the *Gaia*-DR2 distance to each W3 sub-structure.

The *Gaia*-DR2 distance to the W3 complex, $d = 2.05^{+0.10}_{-0.09}$ kpc (indicated by the blue solid line), is compatible within $1-\sigma$ with most of the previous non-kinematic distances. Excluding the distances derived from the trigonometric parallax of maser sources (e.g. Hachisuka et al. 2006 and Xu et al. 2006) the error bars of the *Gaia*-DR2 distance to the entire W3 Complex is significantly smaller than the distances obtained from other works. In addition, the most accurate distances based on the annual parallax of maser emission sources in W3(OH) (1.95 ± 0.04 and 2.04 ± 0.07 kpc) are in agreement with the *Gaia*-DR2 distance to W3(OH), $d = 2.07^{+0.19}_{-0.16}$ kpc, derived using the parallaxes of 5 OB stars associated to that region.

The agreement between the distances available in the literature and the relatively more accurate *Gaia*-DR2 distance allow us to confirm that the OB-type stars listed in Table 2 are indeed high-mass stars located at distances of around ~ 2 kpc.

In a large-scale context, the distance to W3 is also consistent with the distances to the massive clusters located in W4 (IC 1805) and W5 (IC 1848), at distances of 2.3-2.4

(Sung et al. 2017) and 1.9-2.2 kpc (Chauhan et al. 2011), respectively. These three complexes cover a considerable portion of the Perseus arm of about 3 degrees (from 134° to 137°) in the Galactic anti-centre direction, allowing us to set a firm location of the Perseus spiral arm with high confidence.

At a distance of ~ 2.1 kpc, the mean proper motion of the W3 Complex ($\langle \mu_\alpha \cos(\delta) \rangle = -0.786 \pm 0.055$ mas yr $^{-1}$ and $\langle \mu_\delta \rangle = -0.520 \pm 0.062$ mas yr $^{-1}$, see Table 6) leads a to linear velocity of 10.4 ± 0.9 km s $^{-1}$ roughly oriented in the SW direction. We evaluated the mean proper motion of the W3 complex in Galactic coordinates using the transformations available in Sect. 3.1.7 of the *Gaia*-DR2 Documentation release 1.1³. The proper motions in Galactic coordinates are $\mu_\ell \cos(b) = -0.527$ mas yr $^{-1}$ and $\mu_b = -0.768$ mas yr $^{-1}$. The linear velocity components are $v_\ell = -5.6$ km s $^{-1}$ and $v_b = -8.2$ km s $^{-1}$, with a position angle of $\sim 215^\circ$ in relation to the North galactic pole and increasing ℓ values. Such velocities indicate that the W3 Complex has a relatively large tangential motion perpendicularly to the Galactic plane, suggesting that W3 is likely moving out from the Galactic plane. To confirm this scenario, stellar radial velocity measurements are required to properly evaluate the three velocity components UVW in the Galactic coordinate system.

The radial velocity of the gas in the direction of W3 is about -45 km s $^{-1}$ (Xu et al. 2006), which depending on the adopted rotation curve, translates into kinematic distances between 2.9 kpc Reid et al. (2014) and 4.2 kpc Russeil (2003). Xu et al. (2006) reported a difference of ~ 15 km s $^{-1}$ between the rotation velocity of W3(OH) and the velocity expected from Galactic rotation models (e.g. Brand & Blitz 1993). By combining the velocity components on the other directions, those authors found that the peculiar motion of W3(OH) is about 22 km s $^{-1}$. The decomposition of the peculiar motion lead to a tangential velocity of about 15 km s $^{-1}$, which is about twice the tangential velocity of ~ 8 km s $^{-1}$, perpendicular to the Galactic plane, that we found for the whole sample of stars from the W3 Complex (see Sect. 4.2).

W3 is not an exception in terms of peculiar motions or divergence between kinematic and non-kinematic distances. Similar behaviour as that observed in W3(OH) was previously detected in other regions of the outer second quadrant of the Galaxy, where streaming motions with velocities of 15-20 km s $^{-1}$ are well-known (Brand & Blitz 1993; Digel et al. 1996). Baba et al. (2009) presents a list of star-forming regions that exhibits peculiar motions with velocities between 20-30 km s $^{-1}$. Later, Moisés et al. (2011) compared the spectrophotometric and kinematic distances of 35 star-forming regions located at different directions in the Galactic plane. Those authors found that about half of their sample is located at a closer distance than their kinematic distances. More recently, Choi et al. (2014) presented a large-scale study of the distance and proper-motions of star-forming regions in the Perseus arm leading to the conclusion that, in average, the spiral arm is rotating slower than expected from Galactic rotation models. In general, the divergence between the radial velocity predicted by the rotation curves and the observed velocities can be explained by internal pro-

³ <https://gea.esac.esa.int/archive/documentation/GDR2/>

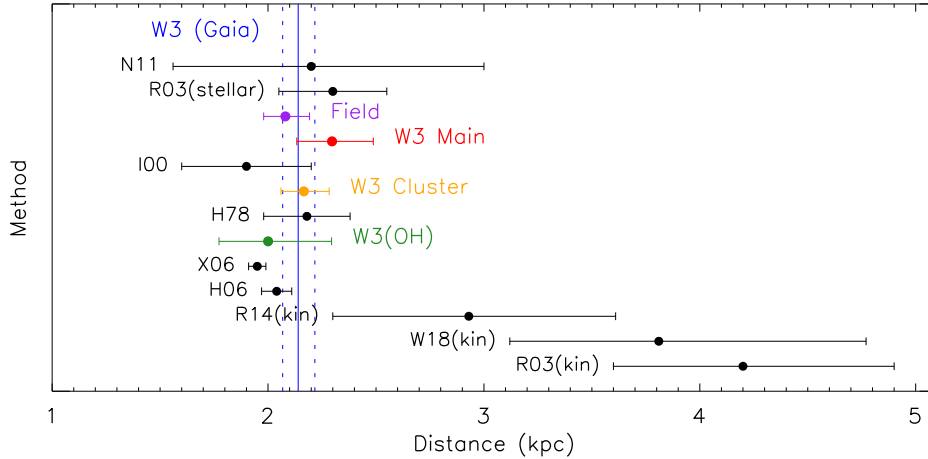


Figure 8. Comparison between distances to the W3 Complex derived in this work and those reported in the literature. The vertical solid and dashed blue lines indicate the *Gaia*-DR2 distance to the W3 Complex and its errors, when considering the large sample of *Gaia*-DR2 sources. The *Gaia*-DR2 distances to each sub-structure and their uncertainties are shown by the coloured dots and their error bars. The black dots and associated errors correspond to the distances reported in Table 1, together with the references shown in the plot.

cesses within the star-forming regions, such as the local stellar winds from high-mass stars (Kudritzki & Puls 2000), or can be caused by external processes, such as the interaction between supernovae and GMCs (e.g. the HB 3 and W3, see Zhou et al. 2016), or fluctuations in the Galactic gravitational potential (Junqueira et al. 2013).

5 CONCLUSIONS

We investigated the *Gaia*-DR2 parallaxes of the OB stellar population of the high-density layer of W3, located in the Perseus Arm, to infer the distance to the complex of H II regions and its main sub-structures. Based on their astrometric parameters, we selected 37 new objects that are likely associated with W3.

(i) Based on the parallaxes of 68 sources and the Exponentially Decreasing Space Density prior from Bailer-Jones (2015), the distance to W3 was estimated in $2.14^{+0.08}_{-0.07}$ kpc, in agreement with previous distances determined through trigonometric parallaxes of masers or spectrophotometric analysis. The distance to W3 based only on the initial sample of 31 OB stars is $2.23^{+0.15}_{-0.14}$ kpc.

(ii) Kinematic distances of the W3 complex are roughly a factor of two larger than the distance obtained from *Gaia*-DR2 parallaxes or distances derived from other non-kinematic methods. Even when adopting different Galactic rotation curves (e.g. Russeil 2003 and Reid et al. 2014), the kinematic distances of the W3 complex range between values of 2.9 and 4.2 kpc, with uncertainties up to 0.7 kpc.

(iii) We further derived the distances to the three main sub-structures of the high-density layer region of W3. The analysis of their distances based on the parallaxes of the OB stars tentatively suggests that they are located at different distances in the line-of-sight. The larger sample of *Gaia*-DR2 sources corroborates this hypothesis with relatively greater accuracy: W3 Main (to the NW) is located at the outer edge of the W3 Complex ($d = 2.30^{+0.19}_{-0.16}$ kpc), the W3 Cluster is at the centre of the W3 complex at a distance

of $d = 2.17^{+0.12}_{-0.11}$ kpc, and the W3(OH) is likely located at the closer edge of the complex, at $d = 2.00^{+0.29}_{-0.23}$ kpc. Combining position of the sub-regions with their distance, the hierarchical scenario of the formation of the high-density layer of W3 is roughly consistent with the assumption that the W3 Cluster triggered the formation of W3 Main and W3(OH), located in the outer and inner edge of the W3 Complex, respectively.

(iv) We computed the distance to W3 using the self-gravitating isothermal Galactic disc prior (Maíz-Apellániz 2001) which is specific for the population of OB stars in the Solar neighbourhood, and confirmed our results obtained with the Exponentially Decreasing Space Density prior (Bailer-Jones 2015). Both priors return consistent results for the W3 Complex due to its location within the Galactic disc.

ACKNOWLEDGEMENTS

The authors thank the anonymous referee who gave very helpful comments and suggestions to improve this work. We thank K. M. Menten and M. Reid for constructive comments and suggestions on this work. We also thank J. Maíz-Apellániz for providing his code to compute distances based on the self-gravitating isothermal Galactic disc prior. FN thanks the Fundação de Amparo à Pesquisa do Estado de São Paulo (FAPESP) for support through process number 2017/18191-8. AD acknowledges FAPESP (2011/51680-6).

This work has made use of data from the European Space Agency (ESA) mission *Gaia* (<https://www.cosmos.esa.int/gaia>), processed by the *Gaia* Data Processing and Analysis Consortium (DPAC, <https://www.cosmos.esa.int/web/gaia/dpac/consortium>). Funding for the DPAC has been provided by national institutions, in particular the institutions participating in the *Gaia* Multilateral Agreement.

REFERENCES

- Astraatmadja T. L., Bailer-Jones C. A. L., 2016, *ApJ*, **833**, 119
- Baba J., Asaki Y., Makino J., Miyoshi M., Saitoh T. R., Wada K., 2009, *ApJ*, **706**, 471
- Bailer-Jones C. A. L., 2015, *PASP*, **127**, 994
- Becker W., Fenkart R., 1971, *A&AS*, **4**, 241
- Bik A., et al., 2012, *ApJ*, **744**, 87
- Blum R. D., Conti P. S., Daminieli A., 2000, *AJ*, **119**, 1860
- Brand J., Blitz L., 1993, *A&A*, **275**, 67
- Cardelli J. A., Clayton G. C., Mathis J. S., 1989, *ApJ*, **345**, 245
- Chauhan N., Pandey A. K., Ogura K., Jose J., Ojha D. K., Samal M. R., Mito H., 2011, *MNRAS*, **415**, 1202
- Choi Y. K., Hachisuka K., Reid M. J., Xu Y., Brunthaler A., Menten K. M., Dame T. M., 2014, *ApJ*, **790**, 99
- Daminieli A., Almeida L. A., Blum R. D., Daminieli D. S. C., Navarete F., Rubinho M. S., Teodoro M., 2016, *MNRAS*, **463**, 2653
- Digel S. W., Lyder D. A., Philbrick A. J., Puche D., Thaddeus P., 1996, *ApJ*, **458**, 561
- Feigelson E. D., Townsley L. K., 2008, *ApJ*, **673**, 354
- Gaia collaboration et al., 2016, *A&A*, **595**, A133
- Gaia collaboration Brown A. G. A., Vallenari A., et al., 2018, preprint ([arXiv:1804.09365](https://arxiv.org/abs/1804.09365))
- Georgelin Y. M., Georgelin Y. P., 1976, *A&A*, **49**, 57
- Ginsburg A., Bally J., Williams J. P., 2011, *MNRAS*, **418**, 2121
- Graczyk D., et al., 2019, arXiv e-prints, Hachisuka K., et al., 2006, *ApJ*, **645**, 337
- Hanson M. M., Conti P. S., Rieke M. J., 1996, *ApJS*, **107**, 281
- Hanson M. M., Kudritzki R.-P., Kenworthy M. A., Puls J., Tokunaga A. T., 2005, *ApJS*, **161**, 154
- Hoag A. A., Johnson H. L., Iriarte B., Mitchell R. I., Hallam K. L., Sharpless S., 1961, Publications of the U.S. Naval Observatory Second Series, **17**, 344
- Hou L. G., Han J. L., 2014, *A&A*, **569**, A125
- Humphreys R. M., 1978, *ApJS*, **38**, 309
- Imai H., Kameya O., Sasao T., Miyoshi M., Deguchi S., Horiuchi S., Asaki Y., 2000, *ApJ*, **538**, 751
- Junqueira T. C., Lépine J. R. D., Braga C. A. S., Barros D. A., 2013, *A&A*, **550**, A91
- Kawamura J. H., Masson C. R., 1998, *ApJ*, **509**, 270
- Kiminki M. M., Kim J. S., Bagley M. B., Sherry W. H., Rieke G. H., 2015, *ApJ*, **813**, 42
- Koukkel M., et al., 2018, *AJ*, **156**, 84
- Kudritzki R.-P., Puls J., 2000, *ARA&A*, **38**, 613
- Kwon S. M., Lee S.-W., 1983, Journal of Korean Astronomical Society, **16**, 7
- Lada C. J., Elmegreen B. G., Cong H.-I., Thaddeus P., 1978, *ApJ*, **226**, L39
- Lindgren L., et al., 2018a, Re-normalising the astrometric chi-square in Gaia DR2, GAIA-C3-TN-LU-LL-124, http://www.rssd.esa.int/doc_fetch.php?id=3757412
- Lindgren L., et al., 2018b, *A&A*, **616**, A2
- López-Corredoira M., 2014, *A&A*, **563**, A128
- Luri X., et al., 2018, preprint, ([arXiv:1804.09376](https://arxiv.org/abs/1804.09376))
- Maíz-Apellániz J., 2001, *AJ*, **121**, 2737
- Maíz Apellániz J., 2005, in Turon C., O’Flaherty K. S., Perryman M. A. C., eds, ESA Special Publication Vol. 576, The Three-Dimensional Universe with Gaia. p. 179 ([arXiv:astro-ph/0411346](https://arxiv.org/abs/astro-ph/0411346))
- Massey P., Johnson K. E., Degioia-Eastwood K., 1995, *ApJ*, **454**, 151
- Menten K. M., Johnston K. J., Wadiak E. J., Walmsley C. M., Wilson T. L., 1988, *ApJ*, **331**, L41
- Moisés A. P., Daminieli A., Figueredo E., Blum R. D., Conti P. S., Barbosa C. L., 2011, *MNRAS*, **411**, 705
- Navarete F., Figueredo E., Daminieli A., Moisés A. P., Blum R. D., Conti P. S., 2011, *AJ*, **142**, 67
- Oey M. S., Watson A. M., Kern K., Walth G. L., 2005, *AJ*, **129**, 393
- Ogura K., Ishida K., 1976, *PASJ*, **28**, 651
- Ojha D. K., et al., 2004, *ApJ*, **608**, 797
- Reid M. J., et al., 2014, *ApJ*, **783**, 130
- Reid M. J., Dame T. M., Menten K. M., Brunthaler A., 2016, *ApJ*, **823**, 77
- Riess A. G., et al., 2018, *ApJ*, **861**, 126
- Roccatagliata V., Bouwman J., Henning T., Gennaro M., Feigelson E., Kim J. S., Sicilia-Aguilar A., Lawson W. A., 2011, *ApJ*, **733**, 113
- Román-Zúñiga C. G., Ybarra J. E., Megías G. D., Tapia M., Lada E. A., Alves J. F., 2015, *AJ*, **150**, 80
- Russeil D., 2003, *A&A*, **397**, 133
- Schönrich R., McMillan P., Eyer L., 2019, arXiv e-prints, Skrutskie M. F., et al., 2006, *AJ*, **131**, 1163
- Stassun K. G., Torres G., 2018, *ApJ*, **862**, 61
- Stead J. J., Hoare M. G., 2009, *MNRAS*, **400**, 731
- Sung H., et al., 2017, *ApJS*, **230**, 3
- Urquhart J. S., Figura C. C., Moore T. J. T., Hoare M. G., Lumsden S. L., Mottram J. C., Thompson M. A., Oudmaijer R. D., 2014, *MNRAS*, **437**, 1791
- Vasilevskis S., Sanders W. L., van Altena W. F., 1965, *AJ*, **70**, 806
- Wenger T. V., Bailer-Jones A. G. A., Andersson L. D., Bania T. M., 2018, *ApJ*, **856**, 52
- Xu Y., Reid M. J., Zheng X. W., Menten K. M., 2006, *Science*, **311**, 54
- Zhou X., Yang J., Fang M., Su Y., Sun Y., Chen Y., 2016, *ApJ*, **833**, 4
- Zinn J. C., Pinsonneault M. H., Huber D., Stello D., 2018, arXiv e-prints,

APPENDIX A: COMPARISON BETWEEN DIFFERENT PRIORS

We compared the distance to the W3 Complex from Sect. 3.3 assuming the self-gravitating, isothermal Galactic disc prior from Maíz-Apellániz (2001), obtained from the study of the distribution of OB stars in the Solar neighbourhood measured by Hipparcos:

$$P(z) = \frac{1-f}{\cosh^2\left(\frac{z+z_\odot}{2h_d}\right)} + f \exp\left(-\frac{1}{2}\left(\frac{z+z_\odot}{h_h}\right)^2\right) \quad (\text{A1})$$

where $z = r \sin(b)$, $b = +1.065^\circ$ is the Galactic latitude of W3, $z_\odot = 20.0$ pc is the position of the Sun above the Galactic plane, f is the fraction of the halo and the disc stellar populations (we set $f = 0$ since the W3 Complex is within the Galactic disc), $h_d = 31.8$ pc and $h_h = 490$ pc are the height-scale of the disc and the halo, respectively, taken from Maíz Apellániz (2005).

Figure A1 presents the PDFs of the distance based on both priors and using the mean parallax of the W3 Complex, $\pi = 0.437 \pm 0.088$ mas from Table 6. The resulting distances and their associated errors are $d = 2.55^{+0.75}_{-0.48}$ kpc and $2.45^{+0.66}_{-0.43}$ kpc for the Maíz-Apellániz (2001) and Bailer-Jones (2015) priors, respectively.

We found that both priors led to similar distances, and the usage of one prior or another does not improve the resulting distance to W3. For this reason, we adopted the EDSD prior from BJ15 in our analysis.

This paper has been typeset from a $\text{\TeX}/\text{\LaTeX}$ file prepared by the author.

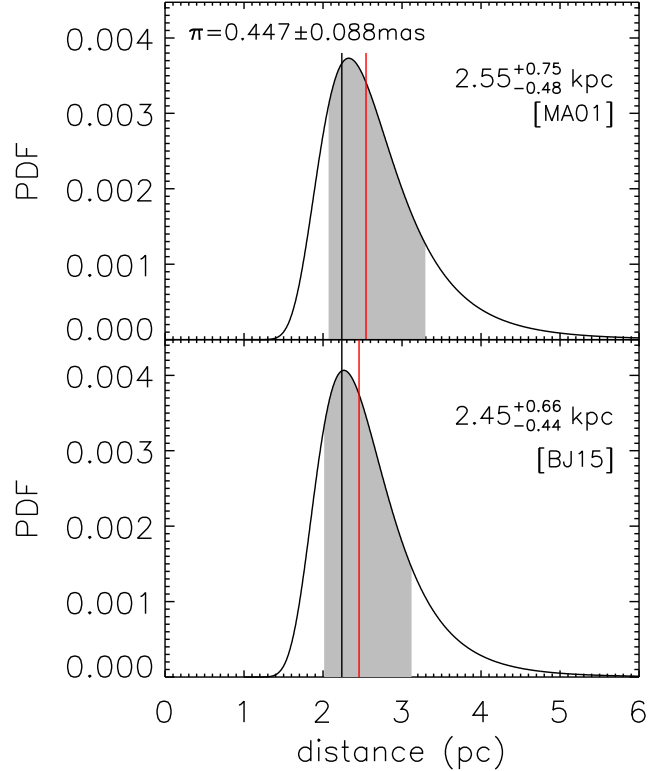


Figure A1. Probability density function (PDF) of the posterior distance estimate based on the mean parallax of the W3 Complex and using the priors from Maíz-Apellániz (2001) (top) and Bailer-Jones (2015) (bottom). The naive inversion of the mean parallax is indicated by the vertical black line. The median value of the PDF is indicated by the red vertical line. The errors correspond to the $1-\sigma$ (68%) confidence interval (shaded grey area).